THE JOURNAL OF PHYSICAL CHEMISTRY A
A JOURNAL OF THE AMERICAN CHEMICAL SOCIETY

pubs.acs.org/JPCA Article

Vibronic Photoexcitation Dynamics of Perylene Diimide: Computational Insights

Hassiel Negrin-Yuvero, Aliya Mukazhanova, Victor M. Freixas, Sergei Tretiak, Sahar Sharifzadeh, and Sebastian Fernandez-Alberti*

Cite This: https://doi.org/10.1021/acs.jpca.1c09484 Read Online

ACCESS | Metrics & More | Article Recommendations | Supporting Information

ABSTRACT: Perylene diimide (PDI) represents a prototype material for organic optoelectronic devices because of its strong optical absorbance, chemical stability, efficient energy transfer, and optical and chemical tunability. Herein, we analyze in detail the vibronic relaxation of its photoexcitation using nonadiabatic excited-state molecular dynamics simulations. We find that after the absorption of a photon, which excites the electron to the second excited state, S_2, induced vibronic dynamics features persistent modulations in the spatial localization of electronic and vibrational excitations. These energy exchanges are dictated by strong vibronic couplings that overcome structural disorders and thermal fluctuations. Specifically, the electronic wavefunction periodically swaps between localizations on the right and left sides of the molecule. Within 1 ps of such dynamics, a nonradiative transition to the lowest electronic state, S_1, takes place, resulting in a complete delocalization of the wavefunction. The observed vibronic dynamics emerges following the electronic energy deposition in the direction that excites a combination of two dominant vibrational normal modes. This behavior is maintained even with a chemical substitution that breaks the symmetry of the molecule. We believe that our findings elucidate the nature of the complex dynamics of the optically excited states and, therefore, contribute to the development of tunable functionalities of PDIs and their derivatives.

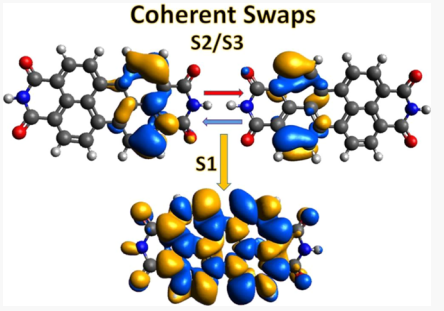

1. INTRODUCTION

Organic solar cells are a lower-cost alternative to traditional silicon-based technologies. The underpinning organic semiconducting materials can be prepared in numerous and flexible ways in a cost-efficient manner, attaining full synthetic control of their solubility and functionalization.[1] To improve the efficiency and lifetime of the materials under operating conditions and design higher-performing devices, it is necessary to understand the fundamental electronic and vibrational (vibronic) dynamics.

Among the large number of conjugated polymers and molecular chromophores serving as optical absorbers in the visible range of solar radiation, perylene diimide (PDI) has received widespread attention[2−5] because of its distinct physical and chemical properties, such as high physical and chemical stability, straightforward synthesis, strong electronic affinity, and adjustable photoelectric properties.[3] Additionally, the functionalization of PDI, on various positions with a wide number of organic chemical groups, opens the possibility to fine-tune physical, optical, electronic, and aggregation properties. PDI-based materials have been applied to a wide variety of applications like fluorescence detection,[6−8] organic field-effect transistors,[9] light-collection materials,[10] light-emitting diodes[11] and solar cells,[12,13] advanced oxidation technology for environmental applications,[14] among others. Moreover, recent advances in material design have enabled PDI-based solar cells to reach PCE > 12%.[15]

A cornerstone in the photophysics of organic conjugated molecules such as PDI is the nonradiative relaxation of coupled excited states, resulting from changes in the electronic wavefunction localization modulated by the induced vibrational dynamics interplaying with thermal structural distortions. Modeling this behavior ultimately requires atomistic nonadiabatic excited-state molecular dynamics approaches. A variety of computational codes have been developed and applied: NEWTON-X,[16−18] SHARC,[19−21] PYXAID,[22,23] NWChem,[24,25] and nonadiabatic excited-state molecular dynamics (NEXMD)[26−28] have been developed to address this task.

The process of energy relaxation is naturally accompanied by intramolecular vibrational energy redistributions accepting an excess of electronic energy. These energy redistributions ultimately define relaxation pathways and frequently involve only a few active vibrations.[29−32] The analysis of the vibronic

Received: November 2, 2021
Revised: January 13, 2022

dynamics and the identification of vibrations actively involved in electronic energy transfer can contribute to the development of models that treat these active modes in a quantum-mechanical way. Generally, these insights can also guide the development of new optical-electronic devices and materials in which the efficiency of energy dissipation can be tuned. Finally, the introduction of chemical substituents into the PDI structure can help tune not only optoelectronic properties but also vibronic dynamics toward controlling energy dissipation and energy-transfer processes. Moreover, vibronic coherence effects can also be modulated.[33] Stronger vibronic couplings with pathways involving fewer vibrational normal modes can better overcome the effects of temperature-dependent static (structural defects) and dynamic (phonon bath coupling) disorder.[34,35]

In the previous contribution,[36] we have compared the electronic energy relaxation after photoexcitation of the PDI monomer and the dimer using the NEXMD package. Here, we explicitly compute the vibrational modes that result in internal energy conversion within the PDI monomer with and without functionalization in order to understand the relationship between vibrational modes and wavefunction localization. The study is organized as follows: in Section 2, we present a brief overview of the computational approach, and methods used to analyze the vibronic dynamics and details of our simulations. We discuss results in Section 3, and finally conclude in Section 4.

2. COMPUTATIONAL METHODS

2.1. NEXMD Background. The NEXMD package has been developed to perform nonadiabatic excited-state molecular dynamics combining mixed quantum-classical algorithms[37,38] with "on the fly" analytical calculations of excited-state energies, gradients, and nonadiabatic coupling terms at the configuration interaction singles (CIS) level with the semiempirical Hamiltonian models. Here, a trajectory surface hopping approach[37,38] is used where nuclei are propagated classically, and the electronic wave function $\psi(t) = \sum_\alpha c_\alpha(t)\phi_\alpha$ is propagated quantum-mechanically using the basis of adiabatic electronic states with wavefunctions ϕ_α:

$$i\hbar\dot{c}_\alpha(t) = c_\alpha(t)E_\alpha - i\hbar\sum_\beta c_\beta(t)\boldsymbol{v}\cdot\boldsymbol{d}_{\alpha\beta} \tag{1}$$

with E_α being the energy of the αth electronic excited state, and $\boldsymbol{d}_{\alpha\beta}$ are the nonadiabatic derivative coupling vectors (NACR) defined as $\boldsymbol{d}_{\alpha\beta} = \langle\phi_\alpha \mid \nabla_r\phi_\beta\rangle$. Details of the NEXMD approach, implementation, advantages, and testing parameters can be found in our previous studies.[26−28]

2.2. Analyses of Transient Exciton Localization and Migration. Exciton spatial localization can be monitored throughout the NEXMD simulations by calculating the evolution in time of transition density matrices expressed in the atomic orbital (AO) basis: $(\rho^{0\alpha})_{ij} = \langle\phi_\alpha \mid c_i^\dagger c_j \mid \phi_0\rangle$,[39] with ϕ_0 and ϕ_α being the wavefunctions corresponding to the adiabatic ground and excited states, $c_i^\dagger$ and c_j correspond the respective creation and annihilation operators acting over AO i and j. The diagonal element $(\rho^{0\alpha})_{ii}$ represents the change in the net charge of the electronic density on AO i during a transition from the ground- to the excited-state α. Consequently, the fraction of $\rho^{0\alpha}$ localized on one side x of the molecule is defined as follows:

$$k_\rho = (\rho^{0\alpha})_x^2 = \frac{\sum_{i\in x}(\rho^{0\alpha})_{ii}^2}{\sum_i(\rho^{0\alpha})_{ii}^2} \tag{2}$$

2.3. Representative NACR and Vibrational Energy Analysis. Representative vectors of nonadiabatic derivative couplings $\boldsymbol{d}_{12}$ for the ensemble of NEXMD simulations are analyzed using the singular value decomposition (SVD) of the matrix $\mathbf{A}$ of dimension $3N \times K$. Here, N is the number of nuclear degrees of freedom, and K is the number of NEXMD simulations featuring an effective $S_2 \rightarrow S_1$ transition (i.e., the hop between the lowest two excited electronic states S_1 and S_2). An effective $S_2 \rightarrow S_1$ transition is defined as the last $S_2 \rightarrow S_1$ transition without subsequent $S_1 \rightarrow S_2$ back-hopping during the rest of the simulation. Matrix $\mathbf{A}$ is built with columns representing $\boldsymbol{d}_{12}$ at the moment of effective $S_2 \rightarrow S_1$ transition in each of the K NEXMD trajectories. Thereafter, the SVD is performed as follows:

$$\mathbf{A} = \mathbf{U}\cdot\mathbf{W}\cdot\mathbf{V}^T \tag{3}$$

where $\mathbf{U}$ is a $3N \times K$ column-orthogonal matrix, and $\mathbf{V}$ and $\mathbf{W}$ are the $K \times K$ diagonal and orthogonal matrices, respectively. We denote $\boldsymbol{d}_{12}^{\mathrm{SVD},\,i}$ as the ith column of the matrix $\mathbf{U}$ with the associated largest value of w_i. The $\boldsymbol{d}_{12}^{\mathrm{SVD},\,k}$ vector or vectors with the largest w_k can then be considered as representative of the ensemble of $\boldsymbol{d}_{12}$ collected from the different NEXMD simulations.

The $\boldsymbol{d}_{12}^{\mathrm{SVD},\,k}$ vectors can be further projected onto the equilibrium normal mode (ENM) basis set evaluated at the optimal geometry of the ground state $(\{\mathbf{Q}_i\}, (i = 1,...,3N-6)$.

$$\boldsymbol{d}_{12}^{\mathrm{SVD},k} = \sum_{i=1}^{3N-6} c_i\mathbf{Q}_i \;(k = 1, 2, ...) \tag{4}$$

with $c_i = \boldsymbol{d}_{12}\cdot\mathbf{Q}_i$.

The velocities associated to each $\mathbf{Q}_i$ can be obtained from the mass-weighted Cartesian displacements $\{\mathbf{q}_j\}$ $(j = 1,...3N-6)$ as follows:

$$\dot{\mathbf{Q}}_i(t) = \sum_{j=1}^{3N} l_{ji}\dot{\mathbf{q}}_j(t)\; i = 1, ..., 3N-6 \tag{5}$$

where l_{ji} are the elements of the linear transformation matrix $\mathbf{L}$ that express the set of $\{\mathbf{Q}_i\}$ on the basis of $\{\mathbf{q}_j\}$. Subsequently, the vibrational kinetic energy $K_i(t)$ associated with a given ENM $\mathbf{Q}_i$ is calculated as follows:

$$K_i(t) = (\dot{\mathbf{Q}}_i(t))^2 \tag{6}$$

and the corresponding total vibrational energy is obtained from the virial theorem, $E_i(t) = 2K_i(t)$. More details on this approach can be found elsewhere.[29]

2.4. Computational Details. The photoexcitation and subsequent electronic and vibrational relaxation of the symmetric pristine-PDI (s-PDI) and the asymmetric substituted-PDI (a-PDI) (see Figure 1a) have been simulated using the NEXMD package using the semiempirical AM1 Hamiltonian model.[40] The NEXMD simulations were performed at constant energy. Initial conditions were collected from 1 ns-long equilibrated ground-state molecular dynamics trajectory of s-PDI and a-PDI at ambient conditions (T = 300 K) with a Langevin thermostat and friction coefficient γ = 20.0 ps^{-1}. Three hundred (300) and six hundred (600) individual NEXMD simulations were performed for s-PDI and a-PDI, respectively. These excited state trajectories were initiated from

https://doi.org/10.1021/acs.jpca.1c09484
J. Phys. Chem. A XXXX, XXX, XXX−XXX

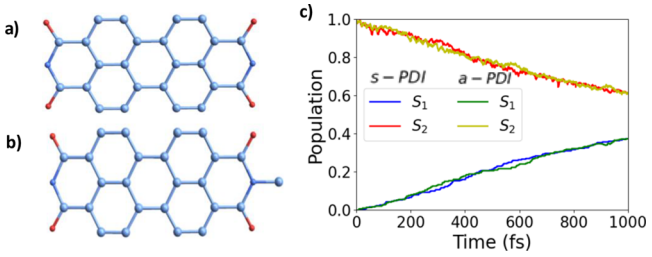

Figure 1. Schematic representation of (a) symmetric (s-PDI) and (b) asymmetric (a-PDI) structures of PDI: C (blue big), N (blue small), O (red). Hydrogen atoms are omitted. (c) Simulated time-resolved average populations of S_1 and S_2 electronic states obtained from the fraction of the trajectory ensemble in each state during NEXMD simulations.

the previously collected initial conditions by instantaneously photoexciting the molecule to the second excited state S_2. A classical time step of 0.5 fs has been used for nuclei propagation in the ground-state dynamics. For the NEXMD simulations, a classical time step of 0.1 fs has been used for nuclei propagation, and a quantum time step of 0.025 fs has been used to propagate the electronic coefficients. Specific treatments of decoherence[41] and trivial unavoided crossings[42] have been considered in these simulations as well.

2.5. Optical Spectra and Vibronic Effects. Ground-state geometries of s-PDI and a-PDI are optimized with the AM1 Hamiltonian in the NEXMD code. The normal modes of molecules are calculated using the AM1 method, as implemented in the Gaussian 16 software package.[43] Time-dependent density functional theory (TDDFT) is utilized to describe the excited-state properties of the molecules, with vibronic effects included via the zero-temperature Franck–Condon (FC) method.[44,45]

3. RESULTS AND DISCUSSION

NEXMD have been performed on symmetric s-PDI and asymmetric a-PDI, shown in Figure 1a, b, respectively. After their initial excitation to the S_2 state, both molecules have very similar relaxation times (Figure 1c). That is, the disruption of the s-PDI symmetry does not affect the nonradiative electronic relaxation. At this point, it is important to mention that electronic relaxation shown in this work differs slightly from the previously reported one,[36] because in the present work, we have added the third excited state, S_3, which is degenerate to S_2, to the NEXMD simulations. Supporting Information Figure S1 shows transition density plots of S_1, S_2, and S_3 states reflecting electronic delocalization of their wavefunctions. S_1 is fully delocalized states, whereas S_2 and S_3 are much more localized transitions with two nodal planes in the middle of the molecule. These near-degenerate S_2 and S_3 states strongly interact during dynamics with periodic localization on molecular sides (Figure S1) before relaxing to the delocalized S_1 wavefunction, as we detail later. Therefore, during the initial phase of our excited-state simulations, adiabatic S_2 and S_3 states actively exchange their populations, and their adiabatic identity is interchanged. This fast back-and-forth exchange takes place in an incoherent way without leading to an effective significant population of S_3. This introduces a dephasing behavior of the S_2 state that slows down its final relaxation to S_1.

As it has been described in Section 2.2, SVD has been performed on the nonadiabatic derivative coupling between S_1 and S_2, $\boldsymbol{d}_{12}$, collected from the different NEXMD simulations at the moment of effective $S_2 \rightarrow S_1$ transitions to obtain the associated representative atomic motions. To confirm the representability of $\boldsymbol{d}_{12}^{\mathrm{SVD},\,i}$, we evaluate their overlap with the original $\boldsymbol{d}_{12}$ ensemble. Figure 2a shows the distribution of the overlap between $\mathbf{s}\text{-}\boldsymbol{d}_{21}^{\mathrm{SVD},1}$ (i.e., the $\boldsymbol{d}_{12}^{\mathrm{SVD},1}$ of s-PDI) and the

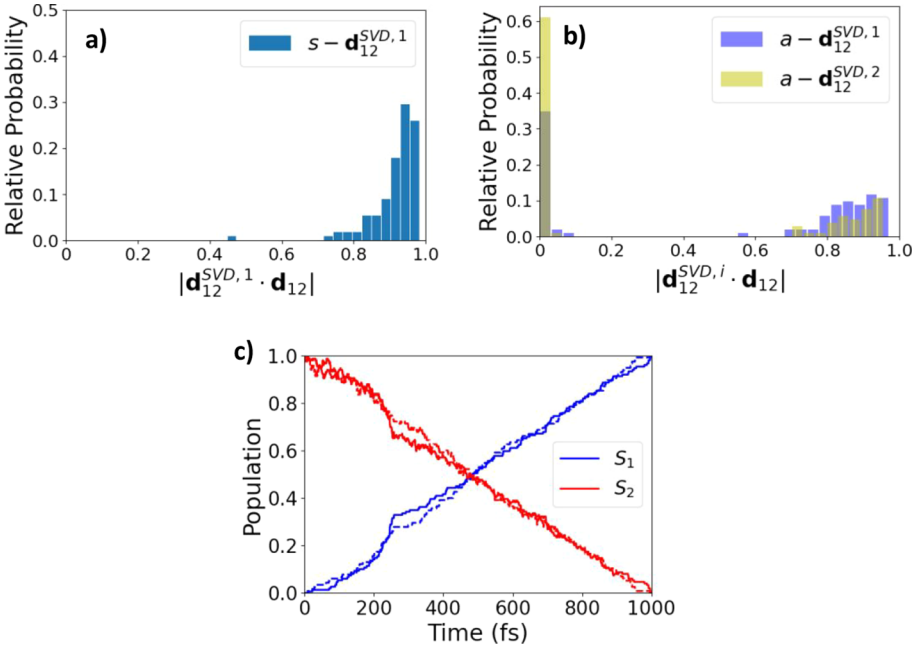

Figure 2. (a) Histogram of the absolute value of the overlap between (a) $\mathbf{s}\text{-}\boldsymbol{d}_{12}^{\mathrm{SVD},1}$ with respect to the original $\boldsymbol{d}_{12}$ obtained during the NEXMD simulations for s-PDI and (b) the same as (a) but for $\mathbf{a}\text{-}\boldsymbol{d}_{1,2}^{\mathrm{SVD},\,i}$ (i = 1, 2) with respect to the originals $\boldsymbol{d}_{1,2}$ obtained for a-PDI. (c) Average populations of S_1 and S_2 electronic states as a function of time, for a-PDI simulations for effective $S_2 \rightarrow S_1$ transitions. Relaxation pathways represented by $\mathbf{a}\text{-}\boldsymbol{d}_{12}^{\mathrm{SVD1}}$ ($\mathbf{a}\text{-}\boldsymbol{d}_{12}^{\mathrm{SVD2}}$) are indicated with solid (dashed) curves.

https://doi.org/10.1021/acs.jpca.1c09484
J. Phys. Chem. A XXXX, XXX, XXX−XXX

originals $\boldsymbol{d}_{21}$. The distribution presents an overlap average value of 0.9. That is, all NEXMD simulations experience the effective $S_2 \rightarrow S_1$ transition through a common energy-transfer pathway along the direction of s-$\boldsymbol{d}_{12}^{SVD,1}$. In the case of a-PDI, shown in Figure 2b, we observe that about half of the simulations follow the energy transfer in the direction of the corresponding a-$\boldsymbol{d}_{12}^{SVD,1}$ and the other half in the direction of a-$\boldsymbol{d}_{12}^{SVD,2}$ with no situations involving a mixture between the two. Here, a-$\boldsymbol{d}_{12}^{SVD,1}$ and a-$\boldsymbol{d}_{12}^{SVD,2}$ hold the same overlap average values of 0.9. Given two distinct pathways dictated by a-$\boldsymbol{d}_{12}^{SVD,1}$ and a-$\boldsymbol{d}_{12}^{SVD,2}$, we therefore split a-PDI simulations in those that involve $S_2 \rightarrow S_1$ effective transitions in these two directions. Figure 2c shows that these two directions of vibronic coupling lead to equivalent relaxation times. In order to clarify this observation, Figure 3 depicts s-$\boldsymbol{d}_{12}^{SVD,1}$ and a-$\boldsymbol{d}_{12}^{SVD,i}$ (i = 1, 2).

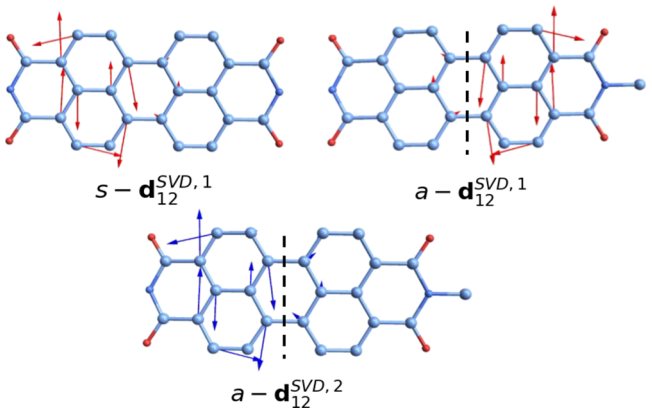

Figure 3. Representation of the different $\boldsymbol{d}_{1,2}^{SVD,i}$ associated with the vibronic couplings for s-PDI and a-PDI nonadiabatic dynamics. The vertical dashed line separates the molecules in the two segments that have the same vibronic dynamics.

We observe that a-$\boldsymbol{d}_{12}^{SVD,i}$ involve equivalent motions but involving different sides of the molecule, separated by a vertical dashed line shown in Figure 3, which collapse only in a single s-$\boldsymbol{d}_{12}^{SVD,1}$ vector in the s-PDI case because of the molecular symmetry.

Further insights into vibronic dynamics concomitant to the electronic energy relaxation can be provided by inspecting the localization of the electronic transition density ($\rho^{0\alpha}$), where α refers to the current state in the simulations. Figure 4a shows histograms of the number of times $\rho^{0\alpha}$ localization changes between the two halves of the molecule during dynamics. This is traced by calculating the fraction of $\rho^{0\alpha}$ localized on one side of the molecules and denoted as k_ρ (see eq 2). An average of about 12 swaps during 1 ps after photoexcitation is observed, either for s-PDI or a-PDI. That is, far from being statically localized in one side of the molecule, $\rho^{0\alpha}$ constantly changes its localization between both halves. The inspection of individual simulations (see Figure 4b) reveals that these changes of localization occur while the molecular system evolves on the S_2 potential energy surface. These slashes stop once the energy is transferred to the S_1 state. The same dynamics is observed for both s-PDI and a-PDI. Analyses of the localization of electronic transition densities of S_1 and S_2 demonstrates (Supporting Information Figure S1) that S_1 is completely delocalized across the molecule, while S_2 is localized on a few specific sites, making it more susceptible to dynamic structural distortions affecting different sides of the molecule. It is worth

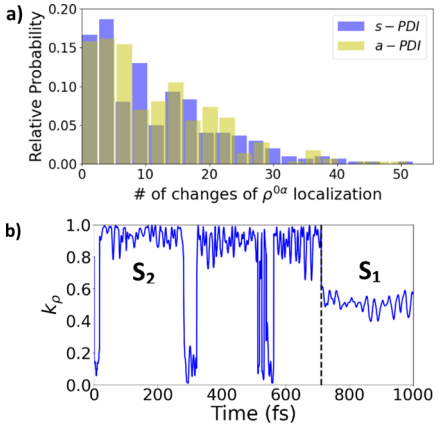

Figure 4. (a) Histogram of the number of times the localization of the electronic transition density ($\rho^{0\alpha}$) changes between the two halves of s-PDI and a-PDI during photoexcited dynamics; (b) fraction of $\rho^{0\alpha}$ (k_ρ) localized on one of the sizes of s-PDI as a function of time for a typical trajectory.

mentioning that these singlet relaxation timescales are significantly faster than the previously reported intersystem crossing lifetimes at the time scale of more than ~400 ps.[46,47]

Thus, after the initial photoexcitation to the S_2 state, the molecule experiences a force in the direction of $\boldsymbol{d}_{12}^{SVD,1/2}$ and alternates the localization of $\rho^{0\alpha}$ between the two sides, leading to swaps throughout the simulations. The evolution of the average fraction of $\rho^{0\alpha}$ (k_ρ) on one side is shown in Figure 5a.

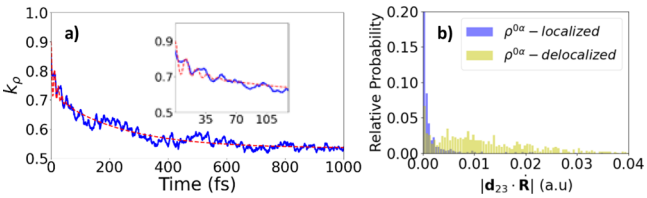

Figure 5. (a) Evolution in time of the average value of k_ρ on the side with the larger initial fraction k_ρ (i.e., $k_\rho > 0.5$ at $t = 0$ fs) for s-PDI; (b) distribution of the absolute values of couplings $|\boldsymbol{v} \cdot \boldsymbol{d}_{23}|$ for s-PDI cases with $\rho^{0\alpha}$ completely localized (i.e., $k_\rho \sim 1$) on one side and delocalized (i.e., $k_\rho \sim 0.5$) between both sides. The curve obtained from the fit to eq 7 is shown by the red-dashed line. The corresponding results obtained for a-PDI are shown in Supporting Information Figure S2.

The selected side corresponds to the larger initial fraction of $\rho^{0\alpha}$ (i.e., $k_\rho > 0.5$ at $t = 0$ fs). The curves are then fitted to the function

$$f(t) = a - \frac{(a-b)}{2}\left\{e^{-t/\tau_1} + \frac{1}{2}\left[1 + \cos\left(\frac{2\pi t}{T}\right)\right]e^{-t/\tau_2}\right\} \quad (7)$$

where T is the period of initial fast oscillations, τ_1 is the decay time, and τ_2 is the vibronic decoherence time. Parameters obtained from the fits are given in Table 1. We observe initial persistent recurrences in both systems, being slightly faster in a-PDI (T = 27.9 fs) compared to s-PDI (T = 27.4 fs). In addition, while both systems have differences in τ_1, similar values of $\tau_2 \sim 18$ fs are obtained. The symmetry of s-PDI requires the identification of the side with a larger initial fraction k_ρ of $\rho^{0\alpha}$. With such an assignment, we observe that across the entire trajectory ensemble, PDI does not randomly

https://doi.org/10.1021/acs.jpca.1c09484
J. Phys. Chem. A XXXX, XXX, XXX−XXX

Table 1. Parameters Obtained from the Fit of Transition Density Dynamics to Eq 7[a]

	s-PDI	a-PDI
a	0.53	0.52
b	0.90	1.0
T (fs)	27.43 ± 0.04	27.93 ± 0.04
τ_1 (fs)	234.8 ± 2.1	185.8 ± 1.6
τ_2 (fs)	18.9 ± 0.6	18.1 ± 0.6

[a] T corresponds to the period of initial fast oscillations, and τ_1 and τ_2 refer to the decay and the decoherence vibronic times, respectively.

change its $\rho^{0\alpha}$ localization but does so coherently in an oscillatory manner. Because of that, the excited vibrational energy is not randomly distributed.

According to Figure 4b, the oscillations observed in Figure 5a are due to molecular motions on the S_2 potential energy surface. In order to gain insight into the origin of this behavior, interactions of S_2 with its quasi-degenerate S_3 state have been analyzed. Figure 5b shows the distribution of the absolute values of couplings $|\boldsymbol{v} \cdot \boldsymbol{d}_{23}|$ (see eq 1) for the cases with $\rho^{0\alpha}$ being completely localized on one side of the molecule and delocalized between both sides (i.e., $k_\rho \sim 0.5$). We can observe that the swaps of $\rho^{0\alpha}$ are in between S_2 and S_3 states that are localized at different sides of the molecule in the equilibrium geometry (see Supporting Information Figure S3 and Movie S1). In the course of nonadiabatic relaxations, distinct vibrational dynamics on the sides of the molecule results in their mixture and crossings, leading to the observed changes in the localization of $\rho^{0\alpha}$, as shown in Figure 4.

It is interesting at this point to analyze $\boldsymbol{d}_{12}^{\mathrm{SVD},\,i}$ in terms of the projection of these vectors onto the normal mode basis. In order to evaluate the number of normal modes that contribute to $\boldsymbol{d}_{12}^{\mathrm{SVD},\,i}$, the participation number, PN, is calculated as follows:[48,49]

$$\mathrm{PN} = \left(\sum_{i=1}^{3N-6} (c_i)^4 \right)^{-1} \tag{8}$$

PN represents the effective number of ENMs that contribute to $\boldsymbol{d}_{12}^{\mathrm{SVD},\,i}$. Values of PN ≈ $3N - 6$ indicate the fully delocalized $\boldsymbol{d}_{12}^{\mathrm{SVD},\,i}$ case with equal contribution from every ENM, whereas PN ≈ 1 corresponds to $\boldsymbol{d}_{12}^{\mathrm{SVD},\,i}$ being identical to a unique ENM. Values of ∼4, 4, and 6 were obtained for s-$\boldsymbol{d}_{12}^{\mathrm{SVD},1}$, a-$\boldsymbol{d}_{12}^{\mathrm{SVD},1}$, and a-$\boldsymbol{d}_{12}^{\mathrm{SVD},2}$, respectively. That is, all of these vectors are spread among only a few normal modes, because only ∼4, 4, and 6 modes are required to describe each of these vectors on the basis of normal modes. The respective sets of normal modes are given in Table 2. Modes #104 and #106 (#113 and #112) provide dominant contributions to s-$\boldsymbol{d}_{12}^{\mathrm{SVD},1}$ (a-$\boldsymbol{d}_{12}^{\mathrm{SVD},1}$ and a-$\boldsymbol{d}_{12}^{\mathrm{SVD},2}$). These vectors are depicted in Figure 6. In the case of s-PDI, modes #104 and #106 correspond to delocalized vibrations within the whole molecule with equally distributed motions for each side (Figure 6a, b). Nevertheless, modes of a-PDI are not symmetrically distributed, with 0.2 and 0.8 (0.8 and 0.2) fractions for #112 (for #113) at the half of the molecule with and without the $-CH_3$ group, respectively (Figure 6c,d). That is, each vibration is more localized on one side or the other. The asymmetry introduced in the PDI molecule by the methyl group disrupts the balance of motions between the two sizes for the modes associated to the vibronic dynamics. It is important to note that, in all cases, the selected

Table 2. Normal Modes with the Highest Overlap Values with Respect to s-$\boldsymbol{d}_{12}^{\mathrm{SVD1}}$ and a-$\boldsymbol{d}_{12}^{\mathrm{SVD1/2}}$[a]

s-$\boldsymbol{d}_{12}^{\mathrm{SVD1}}$		a-$\boldsymbol{d}_{12}^{\mathrm{SVD1}}$		a-$\boldsymbol{d}_{12}^{\mathrm{SVD2}}$	
mode #	overlap	mode #	overlap	mode #	overlap
106 (1797)	0.36	113 (1796)	0.47	112 (1795)	0.32
104 (1795)	0.28	109 (1774)	0.16	109 (1774)	0.22
100 (1728)	0.09	107 (1726)	0.08	113 (1796)	0.13
81 (1421)	0.04	97 (1557)	0.03	88 (1391)	0.04
38 (621)	0.02	105 (1687)	0.02	108 (1760)	0.03
89 (1529)	0.02	92 (1462)	0.02	98 (1576)	0.03
78 (1373)	0.02	41 (616)	0.02	93 (1486)	0.02
115 (3198)	0.02	79 (1252)	0.02	41 (616)	0.02
74 (1273)	0.01	108 (1760)	0.01	77 (1230)	0.02
39 (633)	0.01	88 (1391)	0.01	43 (636)	0.02

[a] Frequencies (cm^{-1}) are given in parenthesis.

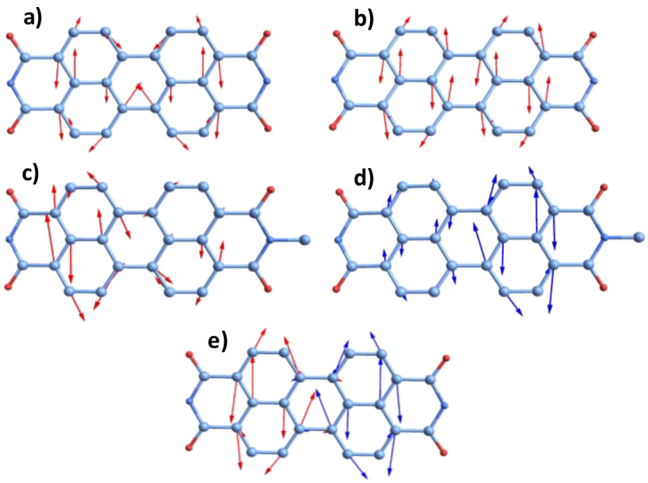

Figure 6. Normal modes providing the main contributions to $\boldsymbol{d}_{12}^{\mathrm{SVD},\,i}$. (a) Mode #104 and (b) #106 contributing to s-$\boldsymbol{d}_{12}^{\mathrm{SVD},1}$; (c and d) modes #113 and #112 associated with a-$\boldsymbol{d}_{12}^{\mathrm{SVD},1}$ and a-$\boldsymbol{d}_{12}^{\mathrm{SVD},2}$, respectively; (e) superpositions #104 + #106 (red) and #104 − #106 (blue).

modes for s-PDI and a-PDI correspond to modes within the range of 1770−1800 cm^{-1}.

We further note that in the s-PDI case, a linear superposition of near-degenerate #104 and #106 modes leads to vibrations completely localized on one or the other side of the molecule (Figure 6c). These localized combinations align better with the direction of the s-$\boldsymbol{d}_{12}^{\mathrm{SVD},1}$ vector, leading to a near-unity overlap (0.98); compare Figures 3 and 6c. Consequently, the projection of s-$\boldsymbol{d}_{12}^{\mathrm{SVD},1}$ onto the normal mode basis in s-PDI, modified including these combinations, reduces the corresponding PN value from ∼4 to ∼2. That is, the linear combination of these two quasi-degenerate modes coincides with the most efficient pathway of energy dissipation. The situation is different in the asymmetric a-PDI case, where the combinations of modes #113 and #112 do not seem to have the same impact.

Next, we identify which vibrational modes participate in optical excitations initially using TDDFT with FC analysis and whether these modes survive during photoexcitation dynamics. The absorption spectra for s-PDI and a-PDI with the contribution of major vibrational modes are shown in Figure 7. The first peaks (set to 0 cm^{-1}, as shown in Figure 7) for both molecules contain mainly 0 → 0 transition.

https://doi.org/10.1021/acs.jpca.1c09484
J. Phys. Chem. A XXXX, XXX, XXX−XXX

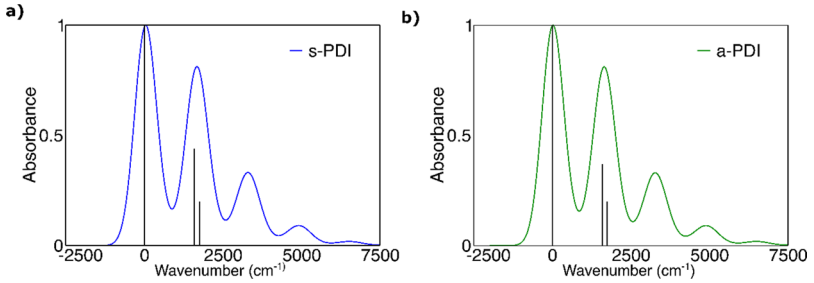

Figure 7. TDDFT-calculated absorption spectrum of (a) s-PDI and (b) a-PDI within the FC approximation. All spectra are normalized such that the highest intensity is set to one. For each molecule, FC modes contributing to vibronic excitation with weight greater than 10% of the maximum are shown.

The second peak at ∼1700 cm^{-1} has contributions from 0 → 1 transition of modes # 94, 95, and 106 for s-PDI and #101, 102, and 113 for a-PDI (Table 3). These modes are shown in Figures 6b, d and 8a, b. Modes #94 and 95 for s-PDI and #101 and 102 for a-PDI are degenerate and do not participate in the vibronic dynamics that takes place during the electronic relaxation. As it has been described previously, vibrational mode #106 for s-PDI and #113 for a-PDI actively participate in energy transfer during dynamics.

Table 3. Normal Modes with the Weight More than 10% of the 0−0 Transition[a]

s-PDI		a-PDI	
mode #	weight	mode #	weight
94 (1604)	0.14	101 (1605)	0.37
95 (1606)	0.44	102 (1611)	0.19
106 (1797)	0.2	113 (1797)	0.20

[a]Frequencies (cm^{-1}) Are Given in Parenthesis.

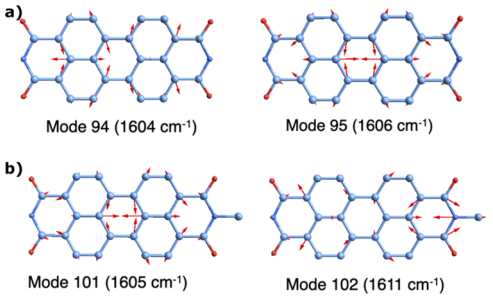

Figure 8. FC modes providing the main contributions (shown as sticks in Figure 7) to vibronic excitation for (a) s-PDI and (b) a-PDI. The other FC modes, that is, mode #106 for s-PDI and #113 for a-PDI are shown in Figure 6.

Because the electronic transitions or hops for the $S_2 \rightarrow S_1$ energy transfer take place at different times across the trajectory ensemble, the concomitant vibrational energy-transfer process cannot be adequately analyzed in terms of the effective simulation time.[29] A more suitable analysis can be achieved by monitoring the vibrational kinetic energy $E_i(\tau)$ (see Section 2.2) as a function of the delay time $\tau = t - t_{hop}$, where t_{hop} is the time of effective nonadiabatic electronic energy transfer from S_2 to S_1 potential energy surface. The delay time τ corresponds to the moment when the nuclear motion activates because of the deposition of electronic energy into vibrations in the direction of the nonadiabatic coupling vector. This is shown in Figure S3, where the average vibrational energy $E_i(\tau)$ is shown as a function of τ for those selected modes that significantly overlap with different $\boldsymbol{d}_{12}^{SVD,\,i}$ vectors, as listed in Table 1. Only those modes with values of $E_i(\tau)$ significantly larger than kT = 26 meV are shown. The rest of the modes are inactive and act as a bath of coupled harmonic oscillators in which the excess of vibrational energy, which remains after the electronic $S_2 \rightarrow S_1$ energy transfer, ultimately spreads at longer times. It is interesting to note that, for s-PDI, the combination of modes #104 + #106 receives nearly the entire amount of vibrational energy in contrast to the combination of modes #104 − #106 and the modes considered individually. That is, the swaps of $\rho^{0\alpha}$, shown in Figure 4, are the result of initially exciting combinations of vibrational normal modes localized at both sizes of the molecule that are responsible for the vibronic dynamics that leads to the ultimate final relaxation to S_1. Therefore, the transient localization of $\rho^{0\alpha}$ within each side is dictated by the structural distortions introduced by these modes.

4. CONCLUSIONS

We have analyzed in detail the vibronic dynamics associated with the nonradiative electronic energy relaxation of the symmetric pristine-PDI (s-PDI) and its asymmetric version (a-PDI) using NEXMD simulations. Both molecules feature similar relaxation timescales and dynamic features. Nevertheless, subtle differences are observed between them. s-PDI experiences the effective $S_2 \rightarrow S_1$ transition through only two generate energy-transfer pathways that involve electronic wavefunctions and vibrational motions strongly localized at the left or right halves of the molecule. In the case of a-PDI, this degeneracy is lifted, and these pathways can be distinguished, although they still account for the same relaxation times. As expected, these two pathways of a-PDI actually represent equivalent motions but involving different sides of the molecule, that is, the size with and without the $-CH_3$ group, respectively.

These specific vibrational dynamics are directly related to the localization of the electronic transition density. We observed that upon photoexcitation, the transition density is not static. Instead, its localization periodically changes between molecular halves, suggesting coherent intramolecular energy migration persisting up to 1 ps. These swaps take place while the system evolves on the potential energy surface formed due to the coupling of degenerate (at the equilibrium geometry) S_2 and S_3 states that are localized at different sides of the molecule. These coherent swaps occur once the energy is transferred to the S_1 state with a fully delocalized wavefunction.

https://doi.org/10.1021/acs.jpca.1c09484
J. Phys. Chem. A XXXX, XXX, XXX−XXX

The analysis of the nuclear motions in terms of vibrational normal modes shows that while for s-PDI the normal modes that mainly contribute to the nonadiabatic coupling are completely delocalized across the entire molecule, modes that contribute to the vibronic dynamics of a-PDI are preferentially localized on one or the other halves of the molecule. In all cases, frequencies of these selected modes coupled to the electronic system lie within the range of 1770−1800 cm^{-1}. A further inspection of the vibrational motions in s-PDI reveals that linear superpositions of the two quasi-degenerate principal vibrational modes fully define energy-transfer pathways compared to the case when these modes are considered individually. This behavior does not occur in a-PDI because the degeneracy is lifted. Altogether, the electronic $S_2 \rightarrow S_1$ energy transfer in both s-PDI and a-PDI funnels mainly through only two normal modes or their linear combinations.

We believe that the identified unique feature characterizing the vibronic dynamics of PDI can be helpful for the future design of functional molecular chromophores with improved performance in organic optoelectronic devices. Given a large variety of PDI-based materials, one can tailor the structure to control transiently coherent electronic and vibrational dynamics that increase the efficiency of intramolecular energy transfer with respect to energy dissipation into heat. Thus, computational modeling of photoinduced processes using a NEXMD framework can contribute to the development of better PDI-based materials and provide novel insights into the rational design of their function, given specific structural modifications.

■ ASSOCIATED CONTENT

Supporting Information

The Supporting Information is available free of charge at https://pubs.acs.org/doi/10.1021/acs.jpca.1c09484.

Electronic transition densities in real space for structures taken from the minimum geometry of the ground state of (a) s-PDI and (b) a-PDI, and (c) structures taken from a typical trajectory of s-PDI; (a) evolution in time of the average value of k_ρ on the side with the larger initial fraction k_ρ (i.e., $k_\rho > 0.5$ at $t = 0$ fs) for a-PDI and (b) distribution of the absolute values of couplings $|\boldsymbol{v} \cdot \boldsymbol{d}_{23}|$ for s-PDI cases with $\rho^{0\alpha}$ completely localized (i.e., $k_\rho \sim 1$) on one side and delocalized (i.e., $k_\rho \sim 0.5$) between both sides; average vibrational energy $E_i(\tau)$ as a function of delay time, $\tau = t - t_{hop}$, relative to the moment of nonadiabatic $S_2 \rightarrow S_1$ energy transfer for modes with the dominant contributions to s-$\boldsymbol{d}_{12}^{SVD,\,i}$ (a) and (b) and a-$\boldsymbol{d}_{12}^{SVD,\,i}$ (c) and (d) (PDF)

Video of the transition density dynamics (MP4)

■ AUTHOR INFORMATION

Corresponding Author

Sebastian Fernandez-Alberti − *Departamento de Ciencia y Tecnologia, Universidad Nacional de Quilmes/CONICET, Bernal B1876BXD, Argentina;* orcid.org/0000-0002-0916-5069; Email: sfalberti@gmail.com

Authors

Hassiel Negrin-Yuvero − *Departamento de Ciencia y Tecnologia, Universidad Nacional de Quilmes/CONICET, Bernal B1876BXD, Argentina*

Aliya Mukazhanova − *Division of Materials Science and Engineering, Boston University, Boston, Massachusetts 02215, United States*

Victor M. Freixas − *Departamento de Ciencia y Tecnologia, Universidad Nacional de Quilmes/CONICET, Bernal B1876BXD, Argentina;* orcid.org/0000-0003-1733-4827

Sergei Tretiak − *Theoretical Division and Center for Integrated Nanotechnologies, Los Alamos National Laboratory, Los Alamos, New Mexico 87545, United States;* orcid.org/0000-0001-5547-3647

Sahar Sharifzadeh − *Division of Materials Science and Engineering and Department of Electrical and Computer Engineering, Boston University, Boston, Massachusetts 02215, United States;* orcid.org/0000-0003-4215-4668

Complete contact information is available at: https://pubs.acs.org/10.1021/acs.jpca.1c09484

Notes

The authors declare no competing financial interest.

■ ACKNOWLEDGMENTS

This work was partially supported by CONICET, UNQ, ANPCyT (PICT-2018-2360). The work at Los Alamos National Laboratory (LANL) was supported by the LANL Directed Research and Development Funds (LDRD) and performed in part at the Center for Integrated Nanotechnologies (CINT), a U.S. Department of Energy, Office of Science User Facility. A.M. and S.S. acknowledge financial support from the National Science Foundation (NSF) CAREER program, under grant number DMR-1847774. This research used resources provided by the LANL Institutional Computing Program and the Boston University Shared Computing Cluster.

■ REFERENCES

(1) Chidichimo, G.; Filippelli, L. Organic Solar Cells: Problems and Perspectives. *Int. J. Photoenergy* **2010**, *2010*, No. 123534.

(2) Li, C.; Wonneberger, H. Perylene Imides for Organic Photovoltaics: Yesterday, Today, and Tomorrow. *Adv. Mater.* **2012**, *24*, 613−636.

(3) Zhang, F.; Ma, Y.; Chi, Y.; Yu, H.; Li, Y.; Jiang, T.; Wei, X.; Shi, J. Self-Assembly, Optical and Electrical Properties of Perylene Diimide Dyes Bearing Unsymmetrical Substituents at Bay Position. *Sci. Rep.* **2018**, *8*, 1−11.

(4) Macedo, A. G.; Christopholi, L. P.; Gavim, A. E. X.; de Deus, J. F.; Teridi, M. A. M.; bin Mohd Yusoff, A. R.; da Silva, W. J. Perylene Derivatives for Solar Cells and Energy Harvesting: A Review of Materials, Challenges and Advances. *J. Mater. Sci.: Mater. Electron.* **2019**, *30*, 15803−15824.

(5) Sharma, V.; Koenig, J. D. B.; Welch, G. C. Perylene Diimide Based Non-Fullerene Acceptors: Top Performers and an Emerging Class Featuring N-Annulation. *J. Mater. Chem. A* **2021**, *9*, 6775−6789.

(6) Feng, X. L.; An, Y. X.; Yao, Z. Y.; Li, C.; Shi, G. Q. A Turn-on Fluorescent Sensor for Pyrophosphate Based on the Disassembly of Cu2+−Mediated Perylene Diimide Aggregates. *ACS Appl. Mater. Interfaces* **2012**, *4*, 614−618.

(7) Lin, J.; Zhu, C.; Liu, X.; Chen, B.; Zhang, Y.; Xue, J.; Liu, J. A Highly Selective and Turn-on Fluorescent Probe for Fe3+ Ion Based on Perylene Tetracarboxylic Diimide. *Chin. J. Chem.* **2014**, *32*, 1116−1120.

(8) Zhang, L.; Zhao, Y.; Wu, Y.; Jiang, Y.; Wang, Q.; Lin, X.; Song, G.; Huang, K.; Yao, Z. An Efficient Approach for Rapid Detection of Polymyxins B Based on the Optically Active Supramolecular Aggregates of Water-Soluble Perylene Diimide. *Sens. Actuators, B* **2020**, *321*, No. 128594.

(9) Gsänger, M.; Oh, J. H.; Könemann, M.; Höffken, H. W.; Krause, A. M.; Bao, Z.; Würthner, F. A Crystal-Engineered Hydrogen-Bonded Octachloroperylene Diimide with a Twisted Core: An n-Channel Organic Semiconductor. *Angew. Chem., Int. Ed.* **2010**, *49*, 740−743.
(10) Hippius, C.; Schlosser, F.; Vysotsky, M. O.; Böhmer, V.; Würthner, F. Energy Transfer in Calixarene-Based Cofacial-Positioned Perylene Bisimide Arrays. *J. Am. Chem. Soc.* **2006**, *128*, 3870−3871.
(11) Oner, I.; Varlikli, C.; Icli, S. The Use of a Perylenediimide Derivative as a Dopant in Hole Transport Layer of an Organic Light Emitting Device. *Appl. Surf. Sci.* **2011**, *257*, 6089−6094.
(12) Duan, Y. W.; Xu, X. P.; Yan, H.; Wu, W. L.; Li, Z. J.; Peng, Q. Pronounced Effects of a Triazine Core on Photovoltaic Performance-Efficient Organic Solar Cells Enabled by a PDI Trimer-Based Small Molecular Acceptor. *Adv. Mater.* **2017**, *29*, No. 1605115.
(13) Kozma, E.; Catellani, M. Perylene Diimides Based Materials for Organic Solar Cells. *Dyes Pigm.* **2013**, *98*, 160−179.
(14) Zhou, W.; Liu, G.; Yang, B.; Ji, Q.; Xiang, W.; He, H.; Xu, Z.; Qi, C.; Li, S.; Yang, S.; et al. Review on Application of Perylene Diimide (PDI)-Based Materials in Environment: Pollutant Detection and Degradation. *Sci. Total Environ.* **2021**, *780*, No. 146483.
(15) Li, M.; Gao, K.; Wan, X.; Zhang, Q.; Kan, B.; Xia, R.; Liu, F.; Yang, X.; Feng, H.; Ni, W.; et al. Solution-Processed Organic Tandem Solar Cells with Power Conversion Efficiencies >12%. *Nat. Photonics* **2017**, *11*, 85−90.
(16) Barbatti, M.; Ruckenbauer, M.; Plasser, F.; Pittner, J.; Granucci, G.; Persico, M.; Lischka, H. Newton-X: A Surface-Hopping Program for Nonadiabatic Molecular Dynamics. *Wiley Interdiscip. Rev.: Comput. Mol. Sci.* **2014**, *4*, 26−33.
(17) Mai, S.; Marquetand, P.; González, L. NEWTON-X. *Wiley Interdiscip. Rev.: Comput. Mol. Sci.* **2018**, *8*, e1370.
(18) Barbatti, M.; Granucci, G.; Persico, M.; Ruckenbauer, M.; Vazdar, M.; Eckert-Maksić, M.; Lischka, H. The On-the-Fly Surface-Hopping Program System Newton-X: Application to Ab Initio Simulation of the Nonadiabatic Photodynamics of Benchmark Systems. *J. Photochem. Photobiol., A* **2007**, *190*, 228−240.
(19) Richter, M.; Marquetand, P.; González-Vázquez, J.; Sola, I.; González, L. SHARC: Ab Initio Molecular Dynamics with Surface Hopping in the Adiabatic Representation Including Arbitrary Couplings. *J. Chem. Theory Comput.* **2011**, *7*, 1253−1258.
(20) Mai, S.; Marquetand, P.; González, L. Nonadiabatic Dynamics: The SHARC Approach. *Wiley Interdiscip. Rev.: Comput. Mol. Sci.* **2018**, *8*, e1370.
(21) Plasser, F.; Gómez, S.; Menger, M.; Mai, S.; González, L. Highly Efficient Surface Hopping Dynamics Using a Linear Vibronic Coupling Model. *Phys. Chem. Chem. Phys.* **2019**, *21*, 57−69.
(22) Akimov, A. V.; Prezhdo, O. V. The PYXAID Program for Non-Adiabatic Molecular Dynamics in Condensed Matter Systemsmics in Condensed Matter Systems. *J. Chem. Theory Comput.* **2013**, *9*, 4959−4972.
(23) Akimov, A. V.; Prezhdo, O. V. Advanced Capabilities of the PYXAID Program: Integration Schemes, Decoherence Effects, Multiexcitonic States, and Field-Matter Interaction. *J. Chem. Theory Comput.* **2014**, *10*, 789−804.
(24) Song, H.; Fischer, S. A.; Zhang, Y.; Cramer, C. J.; Mukamel, S.; Govind, N.; Tretiak, S. First Principles Nonadiabatic Excited-State Molecular Dynamics in NWChem. *J. Chem. Theory Comput.* **2020**, *16*, 6418−6427.
(25) Song, H.; Freixas, V. M.; Fernandez-Alberti, S.; White, A. J.; Zhang, Y.; Mukamel, S.; Govind, N.; Tretiak, S. An Ab Initio Multiple Cloning Method for Non-Adiabatic Excited-State Molecular Dynamics in NWChem. *J. Chem. Theory Comput.* **2021**, *17*, 3629−3643.
(26) Nelson, T. R.; White, A. J.; Bjorgaard, J. A.; Sifain, A. E.; Zhang, Y.; Nebgen, B.; Fernandez-alberti, S.; Mozyrsky, D.; Roitberg, A. E.; Tretiak, S. Non-Adiabatic Excited-State Molecular Dynamics : Theory and Applications for Modeling Photophysics in Extended Molecular Materials. *Chem. Rev.* **2020**, *120*, 2215−2287.
(27) Malone, W.; Nebgen, B.; White, A.; Zhang, Y.; Song, H.; Bjorgaard, J.; Sifain, A.; Rodriguez-Hernan, B.; Freixas, V.; Fernandez-Alberti, S.; et al. NEXMD Software Package for Non-Adiabatic Excited State Molecular Dynamics Simulations. *J. Chem. Theory Comput.* **2020**, *16*, 5771−5783.
(28) Nelson, T.; Fernandez-Alberti, S.; Roitberg, A. E.; Tretiak, S. Nonadiabatic Excited State Molecular Dynamics: Modeling Photophysics in Organic Conjugated Materials. *Acc. Chem. Res.* **2014**, *47*, 1155−1164.
(29) Alfonso-Hernandez, L.; Athanasopoulos, S.; Tretiak, S.; Miguel, B.; Bastida, A.; Fernandez-Alberti, S. Vibrational Energy Redistribution during Donor-Acceptor Electronic Energy Transfer: Criteria to Identify Subsets of Active Normal Modes. *Phys. Chem. Chem. Phys.* **2020**, *22*, 18454−18466.
(30) Lasorne, B.; Sicilia, F.; Bearpark, M. J.; Robb, M. A.; Worth, G. A.; Blancafort, L. Automatic Generation of Active Coordinates for Quantum Dynamics Calculations: Application to the Dynamics of Benzene Photochemistry. *J. Chem. Phys.* **2008**, *128*, 124307.
(31) Gomez, S.; Heindl, M.; Szabadi, A.; Gonzalez, L. From Surface Hopping to Quantum Dynamics and Back . Finding Essential Electronic and Nuclear Degrees of Freedom and Optimal Surface Hopping Parameters. *J. Phys. Chem. A* **2019**, *123*, 8321−8332.
(32) Richings, G. W.; Robertson, C.; Habershon, S. Can We Use On-the-Fly Quantum Simulations to Connect Molecular Structure and Sunscreen Action? *Faraday Discuss.* **2019**, *216*, 476−493.
(33) Schultz, J. D.; Coleman, A. F.; Mandal, A.; Shin, J. Y.; Ratner, M. A.; Young, R. M.; Wasielewski, M. R. Steric Interactions Impact Vibronic and Vibrational Coherences in Perylenediimide Cyclophanes. *J. Phys. Chem. Lett.* **2019**, *10*, 7498−7504.
(34) Cicoira, F.; Santato, C. *Organic Electronics: Emerging Concepts and Technologies*; John Wiley & Sons, 2013.
(35) Brédas, J. L.; Sargent, E. H.; Scholes, G. D. Photovoltaic Concepts Inspired by Coherence Effects in Photosynthetic Systems. *Nat. Mater.* **2016**, *16*, 35−44.
(36) Mukazhanova, A.; Malone, W.; Negrin-Yuvero, H.; Fernandez-Alberti, S.; Tretiak, S.; Sharifzadeh, S. Photoexcitation Dynamics in Perylene Diimide Dimers. *J. Chem. Phys.* **2020**, *153*, 244117.
(37) Tully, J. C. Molecular Dynamics with Electronic Transitions. *J. Chem Phys.* **1990**, *93*, 1061−1071.
(38) Hammes-schiffer, S.; Tully, J. C. Proton Transfer in Solution : Molecular Dynamics with Quantum Transitions. *J. Chem Phys.* **1994**, *101*, 4657−4667.
(39) Tretiak, S.; Isborn, C. M.; Niklasson, A. M. N.; Challacombe, M. Representation Independent Algorithms for Molecular Response Calculations in Time-Dependent Self-Consistent Field Theories. *J. Chem. Phys.* **2009**, *130*, 054111−054127.
(40) Dewar, M. J. S.; Zoebisch, E. G.; Healy, E. F.; Stewart, J. J. P. The Development and Use of Quantum-Mechanical Molecular-Models.76.AM1 - A New General Purpose Quantum-Mechanical Molecular-Model. *J. Am. Chem. Soc.* **1985**, *107*, 3902−3909.
(41) Nelson, T.; Fernandez-alberti, S.; Roitberg, A. E.; Tretiak, S. Nonadiabatic Excited-State Molecular Dynamics : Treatment of Electronic Decoherence. *J. Chem. Phys.* **2013**, *138*, 224111.
(42) Fernandez-Alberti, S.; Roitberg, A. E.; Nelson, T.; Tretiak, S. Identification of Unavoided Crossings in Nonadiabatic Photoexcited Dynamics Involving Multiple Electronic States in Polyatomic Conjugated Molecules. *J. Chem. Phys.* **2012**, *137*, No. 014512.
(43) Frisch, M. J.; Trucks, G. W.; Schlegel, H. B.; Scuseria, G. E.; Robb, M. A.; Cheeseman, J. R.; Scalmani, G.; Barone, V.; Petersson, G. A.; Nakatsuji, H.; et al. *Gaussian 16, Revision C.01*; Gaussian, Inc.: Wallingford CT, 2016.
(44) Improta, R.; Barone, V.; Santoro, F. Ab Initio Calculations of Absorption Spectra of Large Molecules in Solution: Coumarin C153. *Angew. Chem., Int. Ed.* **2007**, *46*, 405−408.
(45) Santoro, F.; Improta, R.; Lami, A.; Bloino, J.; Barone, V. Effective Method to Compute Franck-Condon Integrals for Optical Spectra of Large Molecules in Solution. *J. Chem. Phys.* **2007**, *126*, No. 084509.
(46) Yarnell, J. E.; Davydenko, I.; Dorovatovskii, P. V.; Khrustalev, V. N.; Timofeeva, T. V.; Castellano, F. N.; Marder, S. R.; Risko, C.; Barlow, S. Positional Effects from σ-Bonded Platinum(II) on

https://doi.org/10.1021/acs.jpca.1c09484
J. Phys. Chem. A XXXX, XXX, XXX−XXX

684 Intersystem Crossing Rates in Perylenediimide Complexes: Synthesis,
685 Structures, and Photophysical Properties. *J. Phys. Chem. C* **2018**, *122*,
686 13848−13862.
687 (47) Mohan, A.; Sebastian, E.; Gudem, M.; Hariharan, M. Near-
688 Quantitative Triplet State Population via Ultrafast Intersystem
689 Crossing in Perbromoperylenediimide. *J. Phys. Chem. B* **2020**, *124*,
690 6867−6874.
691 (48) Bell, R. J.; Dean, P.; Hibbins-Butler, D. C. Localization of
692 Normal Modes i n Vitreous Silica, Germania and Beryllium Fluoride.
693 *J. Phys. C: Solid State Phys.* **1970**, *3*, 2111−2118.
694 (49) Taraskin, S. N.; Elliott, S. R. Anharmonicity and Localization of
695 Atomic Vibrations in Vitreous Silica. *Phys. Rev. B: Condens. Matter*
696 *Mater. Phys.* **1999**, *59*, 8572−8585.

https://doi.org/10.1021/acs.jpca.1c09484
J. Phys. Chem. A XXXX, XXX, XXX−XXX